

GaInP/GaAs three-terminal heterojunction bipolar transistor solar cell

Marius Zehender

Universidad Politécnica de Madrid

Simon Svatek

Universidad Politécnica de Madrid <https://orcid.org/0000-0002-8104-1888>

Myles Steiner

National Renewable Energy Laboratory <https://orcid.org/0000-0003-1643-9766>

Ivan Garcia

Universidad Politecnica de Madrid <https://orcid.org/0000-0002-9895-2020>

Pablo Garcia-Linares

Universidad Politécnica de Madrid <https://orcid.org/0000-0003-2369-3017>

Emily Warren

National Renewable Energy Laboratory (NREL) <https://orcid.org/0000-0001-8568-7881>

Adele Tamboli

National Renewable Energy Laboratory (NREL) <https://orcid.org/0000-0003-2839-9634>

Antonio Martí

Instituto de Energía Solar, Universidad Politécnica de Madrid <https://orcid.org/0000-0002-8841-7091>

Elisa Antolín (✉ elisa.antolin@upm.es)

Universidad Politécnica de Madrid

Article

Keywords: Multijunction solar cell, heterojunction bipolar transistor solar cell, tandem photovoltaic device, III-V materials, three-terminal solar cell

Posted Date: July 23rd, 2021

DOI: <https://doi.org/10.21203/rs.3.rs-113488/v2>

License:  This work is licensed under a Creative Commons Attribution 4.0 International License.

[Read Full License](#)

GaInP/GaAs three-terminal heterojunction bipolar transistor solar cell

*Marius H. Zehender[†], Simon A. Svatek^{†#}, Myles A. Steiner[‡], Iván García[†], Pablo García-
Linares[†], Emily L. Warren[‡], Adele C. Tamboli[‡], Antonio Martí[†], Elisa Antolín^{†*}*

[†] Universidad Politécnica de Madrid – Instituto de Energía Solar, Avenida Complutense 30,
28040 Madrid, Spain

[#] Universidad Politécnica de Madrid – Departamento de Sistemas Informáticos, C/ Alan Turing
s/n, 28031 Madrid, Spain

[‡] National Renewable Energy Laboratory (NREL), Golden, CO, 80401, USA

* Corresponding author: elisa.antolin@upm.es

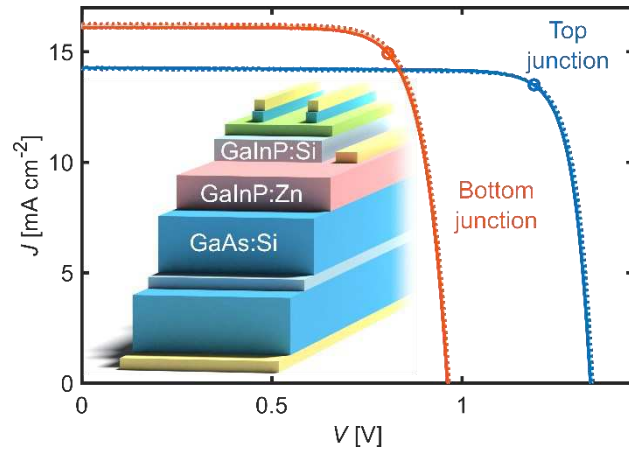
ABSTRACT

We demonstrate a heterojunction bipolar transistor solar cell (HBTSC), a device that exhibits the performance of a double-junction solar cell in a more compact *npn* (or *pnp*) semiconductor structure. The HBTSC concept has the advantages of being a three-terminal device, such as low spectral sensitivity and high tolerance to non-optimal band-gap energies, while it has a lower fabrication and operation complexity than other multi-terminal architectures: it can produce independent power extraction from the two junctions without the need for extra isolating or interconnecting layers between them. The two junctions in our proof-of-concept HBTSC prototype, which is made of epitaxial GaInP/GaAs, exhibit independent current-voltage characteristics under AM1.5G illumination, with respective open-circuit voltages of 1.33 and 0.95 V. The HBTSC opens a new perspective in the understanding of multi-junction devices, and it is an excellent candidate for the application of low-cost fabrication techniques, and for the implementation of III-V-on-silicon tandems.

KEYWORDS

Multijunction solar cell, heterojunction bipolar transistor solar cell, tandem photovoltaic device, III-V materials, three-terminal solar cell

TOC graphic



INTRODUCTION

The detailed balance efficiency limit of an ideal single-gap solar cell is determined solely by the band-gap energy (E_G) of the absorbing material because, when all loss mechanisms have been minimized, the E_G value determines the photocurrent and also sets an upper bound to the open-circuit voltage (V_{OC}).¹ To move towards a higher detailed balance efficiency limit, the combination of semiconductors with different E_G would appear as the most straightforward strategy. However, it is known that using a single-junction formed by two semiconductor regions, one with high band-gap energy ($E_{G,H}$) and the other with low band-gap energy ($E_{G,L}$), does not increase the absolute detailed balance efficiency limit over the single-gap case.^{2,3} For this reason, it has been assumed that the minimal building-blocks for the construction of a multi-gap device are complete single-gap solar cell structures, which may consist of a *pn*-junction (e.g. III-V materials), or an electron-transport-layer/absorber/hole-transport-layer structure (e.g. perovskites). In either case, to fabricate a multi-junction solar cell (MJSC) such building-blocks are stacked, or deposited, one on top of another.⁴ Focusing on the first approach, Figure 1a illustrates the wide-spread example of a double-junction solar cell (2JSC) in which two *pn*-junctions are series-connected by a transparent tunnel diode producing a two-terminal (2T) device.^{5,6} For optimum performance, each sub-cell typically includes passivating layers at their top and rear surfaces (not shown in the figure) because beyond those surfaces there is no ambipolar transport. A three-terminal (3T) version of the classical 2JSC is depicted in Figure 1b, also comprising two complete *pn*-junctions, typically with their corresponding passivating layers, and a contacting layer for the middle terminal.⁷⁻⁹

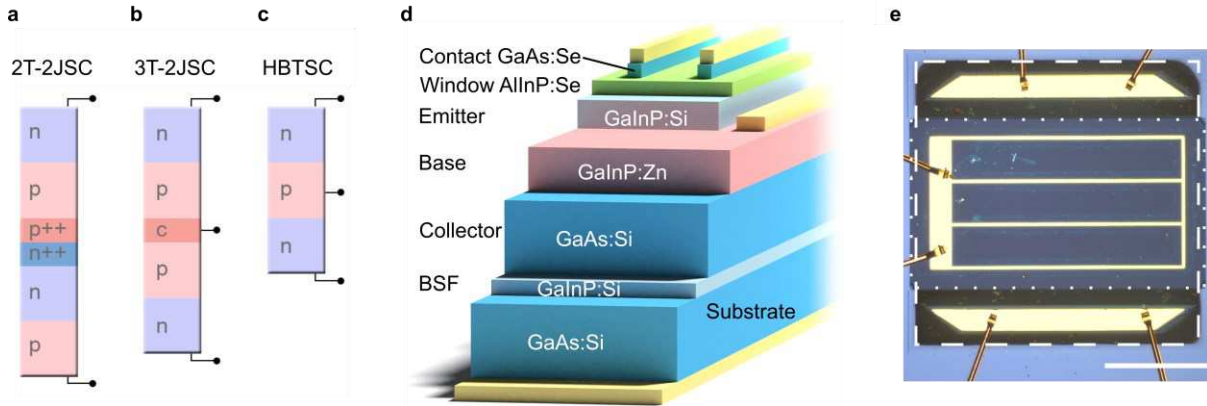


Figure 1. Description of the HBTSC concept and the fabricated prototype. Main semiconductor regions in the structure of a 2T-2JSC (a), a 3T-2JSC with an intermediate conductive layer (b), and the HBTSC device demonstrated in this work (c). d, Schematic cross-section of the GaInP/GaAs HBTSC prototype (sample number MR525). e, Photograph of the HBTSC prototype contacted by wire-bonding. The dashed (dotted) rectangle marks the bottom (top) junction area. Scale bar is 500 μm long. See also Figure S1.

In this work, we demonstrate a new, more compact device concept for the integration of two materials of different E_G into one high-efficiency solar cell. This concept, illustrated in Figure 1c, consists of an *npn* (or *pnp*) structure and, due to the similarity to a transistor, is called heterojunction bipolar transistor solar cell (HBTSC).¹⁰ It is a 3T device in which the top semiconductor region, the emitter (E), has a high band-gap energy $E_{G,H}$ and the bottom region, the collector (C), has a low band-gap energy $E_{G,L}$. The middle, base (B) region, can have an E_G value greater or equal to $E_{G,H}$.¹¹ All three regions (or layers, in the case of an epitaxial or spin-coated device) can absorb light and have ambipolar carrier transport, i.e. all three sustain a quasi-Fermi level (QFL) split. The HBTSC only requires passivation on the top emitter surface and the rear collector surface. Thus, this structure is the most compact 2JSC architecture possible and constitutes a new building-block for multi-junction solar cells.

Traditionally, the current-constrained 2T-MJSC has drawn more attention than multi-terminal approaches. The current-matched architecture holds the absolute record of photoconversion

efficiency, with 47.1% achieved by a six-junction solar cell made of epitaxially-grown III-V materials (measured under concentration of 143 suns; the one-sun record is 39.2%).¹² It has also been applied to 2JSCs introducing emerging technologies, such as the perovskite/silicon tandem,^{13,14} or the wafer-bonding of a III-V and a silicon device.¹⁵ In spite of the high efficiencies demonstrated and the obvious advantages for device interconnection, the current-matched MJSC technology has not been deployed yet in terrestrial applications on a commercial scale because of high cost and low versatility. In this context, the introduction of multiple terminals is attracting a growing interest because it enables technologies with reduced spectral sensitivity and, hence, an increased energy yield,¹⁶⁻²⁰ and it provides more flexibility in the choice of semiconductor materials.²¹ The latter results from a higher tolerance of 3T and 4T architectures against non-optimal E_G values, which facilitates the consideration of economic criteria in the design of MJSC devices. But the positive effect that these factors may have in the final price of electricity can be jeopardized by an increase in fabrication costs, since most 3T and 4T practical devices reported still involve a structural complexity comparable to current-matched 2T devices^{8,22-25} (see Figures 1a and b) to which it is added the extra technological complexity introduced by the additional terminals. The HBTSC concept demonstrated here is material-agnostic and its structural simplicity opens the path to new, low-cost fabrication strategies that can compensate the cost of intricate device processing. For example, while traditional 2T devices require highly-doped, transparent tunnel junctions and traditional 3T devices require highly-doped, transparent contact layers in the middle of the structure, the HBTSC requires neither (see Figure 1c). This, combined with the fact that quaternary or metamorphic layers are also not necessary (because of the flexibility in E_G choice inherent to 3T devices), makes the HBTSC an excellent candidate for the use of emerging materials or, within the III-V material technology, for the application of low-cost epitaxial

techniques, such as high-throughput epitaxy^{26,27} or the sequential growth of many device structures on a single substrate,²⁸ for which metamorphic layers, highly-conductive transparent layers and tunnel diodes may be challenging. Different designs of HBTSCs including emerging low-cost materials, such as metal-halide perovskites or nanowires, have already been proposed.^{29–32} Stringing of multi-terminal devices is also an important challenge that we discuss at the end of the paper, with emphasis on an option that allows the integration of HBTSCs into modules eliminating complex stringing and the extra cost that it could introduce.

Because in the HBTSC the two junctions share the base region, it can be anticipated that the main challenge of this 3T device is to have fully independent power production from both junctions, to enable a straightforward operation, and in particular, to deliver a higher photovoltage at the top (E-B) junction than at the bottom (B-C) junction. The feasibility of the HBTSC concept has been discussed theoretically, and in particular it has been shown that its operation is consistent with the detailed balance model and that the HBTSC, when correctly designed, has the same efficiency limit as a conventional 2JSC with independent junctions.¹⁰ Here, we demonstrate experimentally for the first time HBTSC operation with an epitaxial GaInP/GaAs prototype that exhibits fully independent power extraction from the two junctions.

RESULTS AND DISCUSSION

HBTSC prototype description. The layer structure of our GaInP/GaAs HBTSC prototype is depicted in Figure 1d. It has been grown by metal-organic vapor phase epitaxy (MOVPE) on an *n*-doped GaAs substrate. The design of the base layer is key for the operation of the HBTSC.^{11,33} In this case the base is 565 nm thick and has a concentration of *p*-dopant atoms (Zn) of $6 \times 10^{18} \text{ cm}^{-3}$, notably higher than the *n*-dopant concentration in the emitter and collector (4×10^{17} and $5 \times 10^{17} \text{ cm}^{-3}$; all values determined from secondary ion mass spectroscopy (SIMS) measurements).

Further details are given in the methods section and the Supplementary Information (SI, section S1). Devices like the one shown in Figure 1d were fabricated using photolithography, wet etching and metal evaporation; the metallization of the middle contact will be discussed towards the end. In this proof-of-concept device, the base layer is accessed from the top by etching portions of the emitter. Due to the irregular etching of GaInP and the possibility of underetching,³⁴ large areas are etched around the base contacts (the two horizontal metal pads in Figure 1e). This can be avoided in future prototypes by detaching the epitaxial semiconductor structure from the substrate and contacting the base layer with an interdigitated bottom contact³⁵ (SI, Fig. S12). Following the recently proposed taxonomy for three-terminal tandem solar cells,³⁶ this cell is denoted GaInP/r/GaAs(p/n). The cell has a MgF₂/ZnS anti-reflection coating (ARC) deposited by e-beam evaporation.

Figure 2a shows the current density - voltage (J - V) curves of the two junctions of the HBTSC prototype under illumination with the AM1.5G spectrum, measured with the base contact grounded. All parameters extracted from the J - V curves are compiled in Table 1, together with the parameters extracted from the fitting of the dark J - V curves to a two-exponential model (shown in the SI, Section S7). To discuss the photocurrent densities and conversion efficiencies, the particular geometry of this device must be taken into account. We will introduce that discussion later and will first focus on the interpretation of the J - V curves as proof-of-concept experiment for the HBTSC concept.

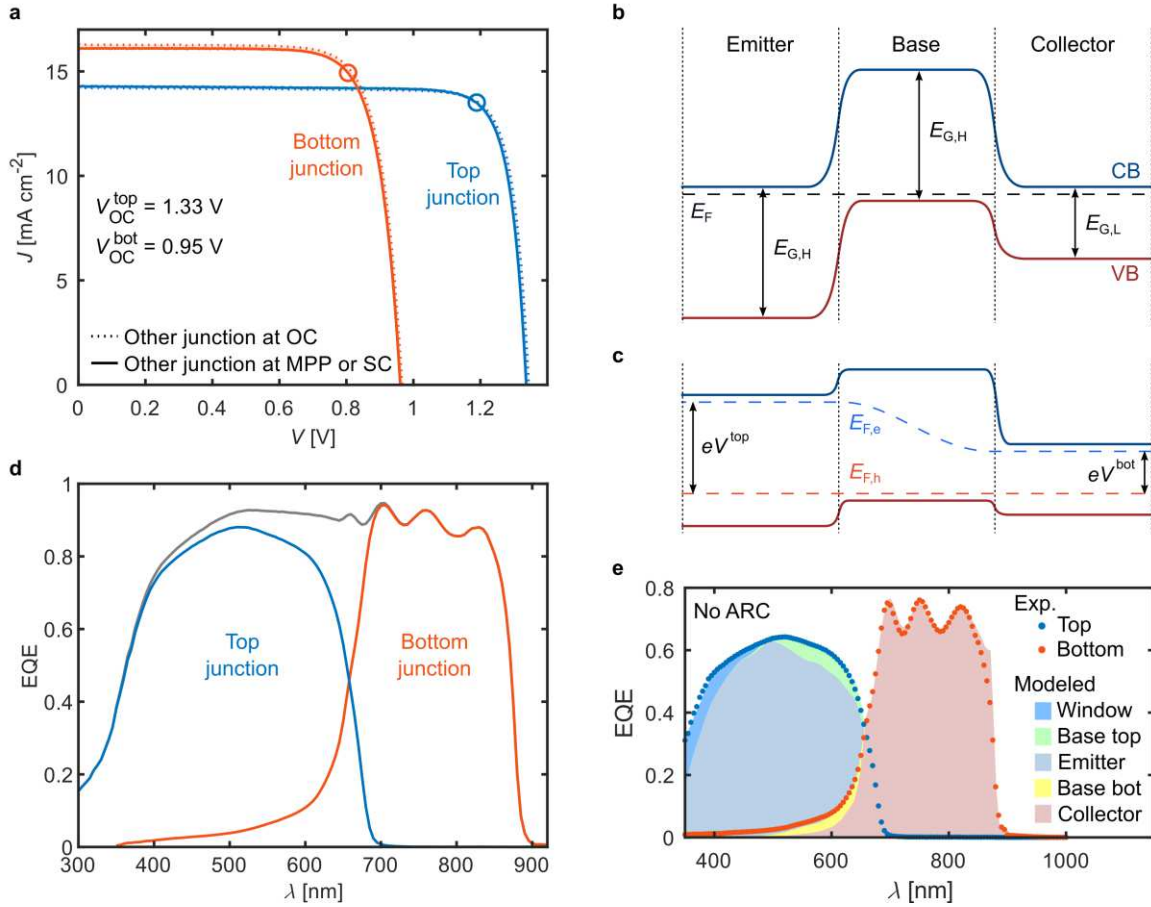


Figure 2. Characterization of the HBTCS prototype as solar cell (sample number MR525). **a**, J - V curves of both junctions at 25°C under AM1.5G spectrum (the area considered is the illuminated area of each junction). A dotted (solid) line means that the other junction was in OC (at the MPP or SC) when the curve was measured. MPPs of the curves plotted with solid lines are marked with circles. The V_{OC} values in the inset correspond to the characterization when the junction that is not being measured is at the MPP. **b- c**, Ideal band diagram of an HBTCS in equilibrium (**b**) and under illumination and a voltage bias V (**c**). E_F is the Fermi level, and $E_{F,e}$ and $E_{F,h}$ are the electron and hole quasi-Fermi levels under illumination. $E_{G,H}$ and $E_{G,L}$ are the high- and low band-gap energies (in our case, the E_G 's of GaInP and GaAs). See also Figure S2. **d**, Experimental EQEs of both junctions. The EQEs are representative of a region of the cell where the bottom junction is fully covered by the top junction. **e**, Experimental EQEs of the HBTSC prior to the deposition of the ARC (solid circles) together with the modeled EQE (colored areas). The window and emitter layers contribute to the EQE of the top junction, and the collector layer to the bottom junction. The modelling shows that the base layer contributes with two EQE components, one that is collected by the top junction (green area) and another collected by the bottom junction (yellow area). See also Figures S4-S6.

Table 1. Parameters of the HBTSC prototype under AM1.5G illumination, extracted from Figure 2a, and in the dark, extracted from the fitting of the dark curves to a two-exponential model including resistive components (series resistance, R_s , and parallel resistance, R_p). The dark curves are shown in the SI, Section S7.

Parameter	Bottom junction	Top junction
Illuminated area [mm ²]	1.57	1.03
V_{OC} [V]	0.95	1.33
J_{SC} [mA cm ⁻²]	16.0	14.2
P_{MPP} [mW cm ⁻²]	11.9	15.9
FF [%]	78.0	84.3
η [%]	11.9 ± 1.3	15.9 ± 1.5
Dark area [mm ²]	1.93	1.16
J_{01} [A cm ⁻²]	$< 10^{-20}$	$\leq 1.5 \cdot 10^{-25}$
J_{02} [A cm ⁻²]	$3.5 \cdot 10^{-10}$	$1.5 \cdot 10^{-12}$
n	2.2	2.4
R_s (dark) [Ω cm ²]	< 0.2	0.8
R_p [Ω cm ²]	$> 1 \cdot 10^9$	$> 3 \cdot 10^8$

Proof of concept of the HBTSC. In Figure 2a, the V_{OC} of the top junction (V_{OC}^{top}) is 380 mV greater than the V_{OC} of the bottom junction (V_{OC}^{bot}). This difference is comparable to the one found between single-junction devices made of GaInP ($E_{G,H} = 1.84$ eV) and GaAs ($E_{G,L} = 1.42$ eV),^{22,37–39} even though in our case the two junctions share a 565-nm-thick semiconductor layer. Also, the J - V curve of either junction is not affected by the working point of the other junction. Crosstalk between sub-cells has been found in other types of three-terminal solar cells.^{17,23,40} Here, conversely, the J - V curves measured for one junction while the other junction was in open circuit (OC, dotted lines) are almost indistinguishable from the curves (solid lines) measured when the other junction was biased at a voltage between maximum power point (MPP) and short-circuit (SC). The small difference in short-circuit current density (J_{SC}) between the two curves of the

bottom junction in Figure 2a can be explained by the presence of luminescent coupling, which is frequently observed in conventional MJSCs made of high-quality III-V semiconductors when the top junctions are biased close to their V_{OC} .⁴¹⁻⁴³ Further characterization of this effect can be found in the SI, Section S6.

The difference between the V_{OC} s of the top and bottom junctions in Figure 2a can be understood with the help of the ideal band diagrams depicted in Figure 2b (HBTSC in equilibrium) and 2c (HBTSC under illumination and forward voltage bias on both junctions). In Figure 2c it is apparent that the quasi-Fermi level (QFL) split ($E_{F,e} - E_{F,h}$), and thus the output voltage, can be larger in the top junction than in the bottom junction owing to a bending of the minority carrier QFL ($E_{F,e}$) across the base region. If the bending took place in the majority carrier QFL ($E_{F,h}$), the E and C terminals would be at the same voltage, i.e., the output voltages of the two junctions would be equal (see SI, Section S2), in disagreement with our experimental findings. Having determined that the bending takes place in the minority QFL is important because a QFL gradient is related to an increase in the entropy generation rate of the device. Under constant temperature, the additional entropy generation term is proportional to $J_i \cdot \nabla E_{Fi}$, where J_i and E_{Fi} are the current density and QFL associated to carrier i (electrons or holes).⁴⁴ This entropy generation term is probably easier to understand through its associated power loss, a resistive loss term of the form $J \cdot \Delta V$. In a device where a high voltage was achieved at the expense of bending the majority carrier QFL, this power loss would be substantial - because of the large associated current density - and a degradation of the fill factor (FF) would be unavoidable. This is the case in a single-junction solar cell consisting of a heterojunction formed by two semiconductors with band-gap energies $E_{G,H}$ and $E_{G,L}$, which is the ultimate reason why the efficiency limit of heterojunction solar cells does not exceed the absolute efficiency limit of single-gap solar cells.³

The lack of crosstalk between junctions observed in our HBTSC prototype is relevant not only because it facilitates the operation of this 3T device – for example, by ensuring straightforward MPP tracking – but also because it rules out two important mechanisms of resistive power loss. A possible origin of crosstalk can be significant carrier injection from the emitter into the base, analogous to what is observed in heterojunction bipolar transistors, which can be caused, in the HBTSC case, by a non-optimal design of the base layer.^{10,11} A significant injection of carriers (electrons in the case of our *npn* structure) from the emitter into the base would imply a non-negligible current density J_e associated with the bent minority carrier QFL, and consequently, a resistive power loss. A second possible origin for crosstalk between junctions is a high resistance that opposes the lateral flow of holes through the base,³³ which would involve a gradient of the majority carrier QFL, with similar consequences on the power production of the HBTSC. This second possibility is discussed in more detail towards the end of the paper.

The difference in V_{OCs} between top and bottom junction in our HBTSC prototype, which indicates that the minority carriers are supporting the QFL gradient, and the negligible crosstalk between junctions, which rules out carrier injection, imply that in the base of our devices the current density associated to the bent QFL, J_e , is very small and, accordingly, the associated power loss term can approach zero. Thus, the achievement of a large V_{OC}^{top} is compatible with a high FF.^{10,45} The absence of a power loss related to the QFL bending in our HBTSC prototype is possible by virtue of the extra terminal and the three-layer structure, and also because the particular layer design of this device minimizes the equilibrium minority carrier density in the base region to avoid carrier injection, which can be realized by implementing a larger E_G and/or a higher doping level in the base layer than in the emitter¹¹ (in our prototype, it is achieved through the latter). In this respect, we would like to emphasize that the HBTSC approach is radically different from monolithic three-

terminal devices previously reported with back-to-back p-n-n-p⁷ or n-p-p ($\sim 3 \mu\text{m}$)-p-n^{8,9} structures. The notion that a correct QFL bending in a thin, optically-active base can ensure independent current extraction from the two junctions is not only conceptually insightful and does not only expand the design space for multi-junction solar cells, but it can also lead to a notable reduction in semiconductor material use and growth time in three-terminal devices, two factors that have an impact on cost.²²

Device performance of the HBTSC prototype. Now we will analyze the J - V curves in Figure 2a and the data in Table 1 from the point of view of device performance. Estimating the total efficiency of this HBTSC prototype is complicated by the difficulties in accurately defining the cell areas. First, no effort was made here to minimize the metal contact pad areas, which therefore introduces shadow losses that would not be present in a more optimized design. Second, the larger area of the bottom cell means that some fraction of the bottom cell is directly illuminated by light that is unfiltered by the top cell, as is described in Steiner *et al.*⁸ This effect likely has a more limited impact on our device than in Steiner *et al.*⁸ because the region where the bottom junction is exposed has a relatively low external quantum efficiency (EQE) in the short-wavelength range due to strong surface recombination. Nevertheless, the unfiltered area would tend to increase the current collection in the bottom junction by as much as 13%. Using the illuminated area of each cell, we estimate an upper limit on the efficiency of this proof-of-concept device to be $(27.8 \pm 2.9)\%$, with 15.9% produced at the top junction and 11.9% produced at the bottom junction. More discussion can be found in the SI, Section S3. We have shown elsewhere³⁵ that HBTSC devices can be fabricated with interdigitated bottom contacts (base/collector) instead of implementing top contacts for the base if the device is removed from the epitaxial substrate. Therefore, in optimized

HBTSC devices the shadowing factor is expected to be similar to that of conventional MJSCs and the efficiency to be a more straightforward determination.

The absolute values of V_{OC} s and FFs observed in our HBTSC prototype, particularly in the bottom junction, are slightly lower than the values reported for current efficiency-record single-junction GaInP and GaAs devices.^{38,40} However, this small degradation cannot be attributed to any effect related to the HBTSC structure because each of these values is independent of the working point of the junction that is not being measured. The V_{OC} and FF values are explained by slightly high dark saturation currents, J_{02} , associated to the exponential with ideality factor $n \sim 2$ in both junctions (see Table 1). As we will see later, the origin is the additional recombination introduced mostly by the non-optimized implementation of the base contact in this proof-of-concept devices, which affects especially the bottom junction, and which can be eliminated through technological development in future devices.

Figure 2d shows the external quantum efficiency (EQE) of the HBTSC prototype. This curve corresponds to the region of the device where the layer structure is complete (the contribution of the region where there is no emitter has been eliminated by comparing two devices with different geometries, see SI Section S4). The EQE is comparable to the ones reported for classical GaInP/GaAs 2JSCs⁴⁶ and it does not change if the voltage of the junction that is not being measured varies between SC and OC. An interesting question about the operation of this device is whether the absorption in the base layer can contribute to the extracted photocurrent. To answer it, in Figure 2e we show the fitting of the experimental EQE to a theoretical model.⁴⁷ To eliminate unnecessary variables, we have chosen for this analysis the EQE of the device prior to the deposition of the ARC. The solid circles are the experimental values, and the modeled contributions of the different layers are represented by colored areas. To calculate the collection

of photocurrent we solved the one-dimensional continuity equations for minority carriers adapting the approach proposed by Hovel ⁴⁸ for single-junction solar cells to the layer structure of an HBTSC. The calculation takes into account the multiple reflections and interference of the light in the multilayer structure. More details on the model are given in the methods section and the parameters used to fit the EQEs are given in Table 2. Figure 2e shows that a small but non-negligible portion of the photocurrent originates in the base, and that it is collected by both junctions (the green area marks the contribution to the top junction, and the yellow area marks the contribution to the bottom junction). The relatively thin emitter in this device (485 nm) allows a clear identification of the base contributions, which can be finely fitted by choosing suitable values of base minority carrier mobility and diffusion length (μ_B , L_B). The possibility of efficiently collecting photogenerated carriers from the base will be relevant in the future design of compact, high-efficiency HBTSC structures.

Table 2. Fitting parameters for the EQE model shown in Figure 2e: layer thickness (d) extracted from the modelling of the sample reflectance measured during growth, doping level (N) extracted from SIMS characterization, minority carrier diffusion length (L), minority carrier mobility (μ) and equivalent surface recombination velocities (S_{eq}) at the front of the emitter and the rear of the collector.

	Emitter	Base	Collector
d [nm]	485	565	3000
N [cm ⁻³]	4×10^{17}	6×10^{18}	5×10^{17}
L [nm]	820	400	6000
μ [cm ² V ⁻¹ s ⁻¹]	35	300	200
S_{eq} [cm s ⁻¹]	100	-	0

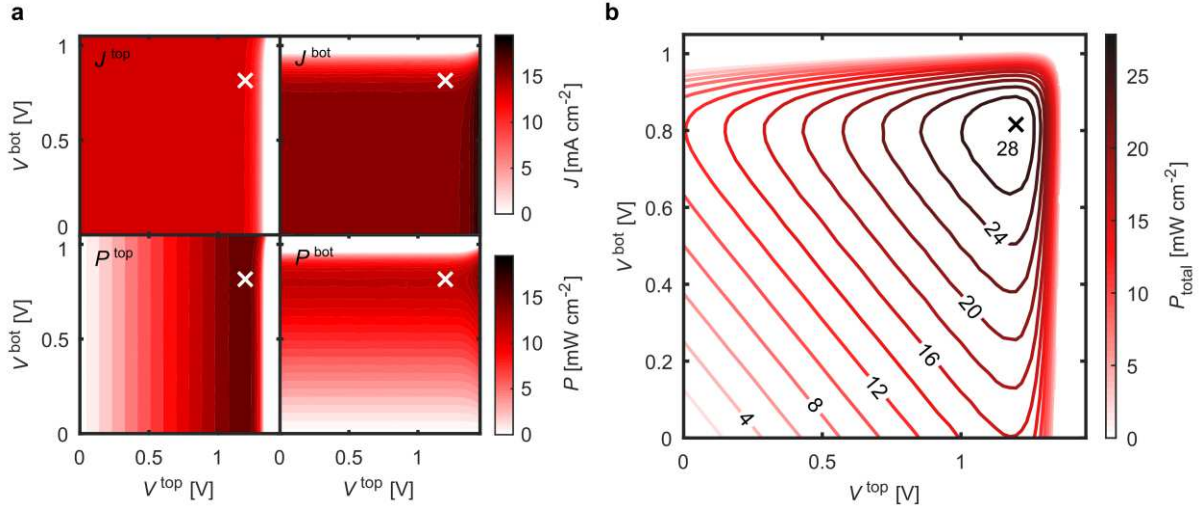


Figure 3. Three-terminal characterization of the HBTSC prototype under AM1.5G spectrum. a, upper two plots: J measured through each junction as a function of the top junction bias (V^{top}) and the bottom junction bias (V^{bot}). The MPP is marked by a white cross. Lower two plots: Same for the output power (P). **b,** Total HBTSC efficiency as a function of V^{top} and V^{bot} . See also Table S1 for area definitions and Figure S7 for dark J - V curves.

To characterize the operation of a three-terminal solar cell under AM1.5G illumination it is useful to measure J on each junction as a function of both voltages, V^{top} and V^{bot} , and plot J and output power (P) maps as the ones shown in Figure 3a. Such plots help identify the possible interaction between sub-cells;^{17,23,40} a detailed description of how to interpret them is given in Warren *et al.*³⁶ In such graphs, negligible crosstalk between cells results in J^{top} and P^{top} being invariant with respect to V_{bot} , i.e. the contour lines would be perfectly vertical with our choice of axes. Similarly, negligible crosstalk leads to the contour lines in our J^{bot} and P^{bot} plots being horizontal. And this is indeed the case in Figure 3a for the V - V area between SC and OC, including the MPP (white cross), which corroborates that in our HBTSC prototype crosstalk between junctions is negligible in photovoltaic operation under the AM1.5G spectrum, and also under low irradiance conditions. In this discussion we have ignored the effect of luminescent coupling, which in our device is

observed in the small increase in J^{bot} when $V^{\text{top}} \geq V_{\text{OC}}^{\text{top}}$ (see the contour lines bending in the upper-right corner of the J^{bot} and P^{bot} plots). Figure 3b shows a map of total device power (P_{total}) obtained from the sum of the P maps in Figure 3a under AM1.5G spectrum. The maximum P_{total} is $27.8 \pm 2.9\%$, achieved for the MPP (0.82 V, 1.20 V), marked with a black cross. It must be remembered that for this proof-of-concept device, to calculate the current density we have only considered the illuminated areas.

Technology of the intermediate contact. From a technological point of view, the metallization of the base contact could be seen as the Achilles' heel of the HBTSC concept. For the contact to become ohmic, especially if the semiconductor has a large band gap energy, an annealing process is required that enables the diffusion of a metallic species, e.g. Zn, to increase the doping level locally. However, it is well-known that annealing results in the formation of intermetallic compounds and strong diffusion of undesired metallic species, e.g. Au, into the semiconductor layer, leading to the formation of point-defects and even extended metal protusions.^{49,50} For this reason, solar cells made of III-V epitaxial materials usually include a highly-doped contact layer over the window layer that serves as a buffer for the metal diffusion. However, the epitaxial structure of an HBTSC cannot include a contact layer for the base terminal. If the metal is deposited on top of the base layer and annealed, diffusion leads to the situation illustrated in Figure 4a, which we will call a direct contact. We have circumvented this problem in our prototypes by implementing the contact as illustrated in Figure 4b, which we will call a compensated contact. In this strategy, the emitter is not fully removed, leaving a thin layer in which the n -doping is compensated and exceeded by Zn atoms from the metallic layers that migrate during the annealing, so that this semiconductor region behaves as a p -doped contact layer and the quality of the base layer is not compromised.

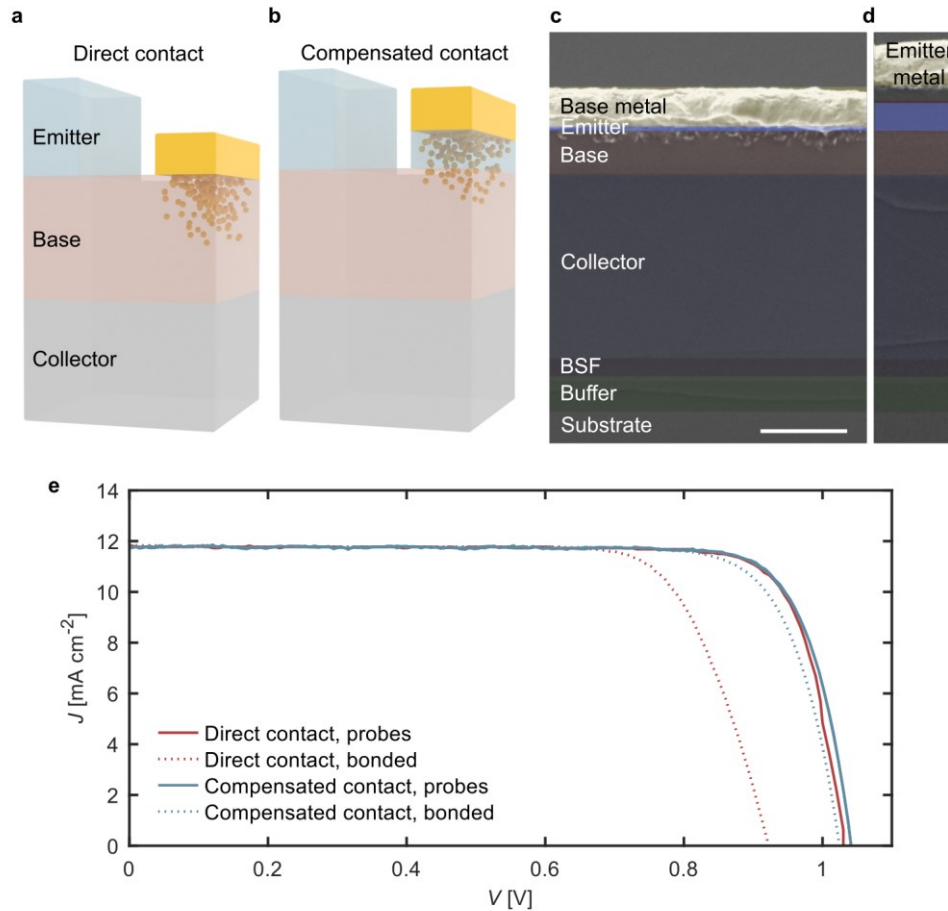


Figure 4. Compensated base contact. **a-b**, Comparison between the fabrication of a direct contact (**a**), where the metal particles diffuse strongly into the base layer during annealing, and a compensated contact (**b**) where a portion of the emitter is not removed before depositing the metal and it becomes compensated during the annealing. **c-d**, Cross-sectional SEM images of a compensated base contact (**c**) and an emitter contact (**d**). Scale bar is 1 μm long. The original thickness of the compensated portion of the emitter below the base metallization and the contact layer below the emitter metallization were 100 nm and 250 nm, respectively, before the metal was evaporated and annealed. **e**, AM1.5G J - V curves of the bottom junction of two HBTSC prototypes made of the same epitaxial structure (this structure has thinner emitter and collector layers than the one used in Figure 2a, which explains the lower photocurrent). Blue lines correspond to a device with compensated base contacts and the red line to a device with direct base contacts. A dashed line means the measurement was taken with probes, and a solid line means it was performed after bonding micro-wires on to the metal. See also Figure S8.

To implement the compensated contact, we first estimated (see SI Section S8) from SIMS of test samples that a thickness between 150 and 250 nm of n-type GaInP becomes p-type GaInP if we

deposit an Au/Zn/Au (15/40/500 nm) metal structure on top and apply high-temperature annealing (420 °C for 180 s). In our HBTSC prototypes, we partially etched the emitter at the base terminal location, leaving a 100 nm-thick layer, and applied the described recipe. Then, we isolated the contact with a second etch around the metal pad. To fabricate the emitter contact, AuGe/Ni/Au (85/25/500 nm) were deposited by thermal evaporation on top of the 250 nm-thick contact layer and the same annealing was applied. Figures 4c and 4d show cross-sectional scanning electron microscope (SEM) images of both contacts. In the compensated base contact, a layer of intermetallic alloy was formed during annealing which did not reach the base region, although it did consume a great part of the compensated layer, which was reduced to less of its original thickness (blue colored region). Also, defects are visible in a region of the base layer which is limited to the uppermost 250-300 nm.

Figure 4e illustrates the superior performance of compensated contacts compared to direct contacts. The plot contains illumination J - V curves of the bottom junction of two HBTSC prototypes made from the same epitaxial structure, one fabricated with a direct contact on the base layer (red curves) and the other with a compensated contact (blue curves). When measured with probes, the direct contact shows an ohmic behavior at first, but it is unstable (solid red curve). The device quickly degrades if it is measured repeatedly or when a micro-wire is bonded to the metallic layer applying ultrasounds and pressure (dotted red curve). On the other hand, the compensated contact produces when measured with probes slightly superior V_{OC} and FF than the best curves obtained with direct contacts, and remains stable over time, showing only a slight degradation after wire-bonding. Although Figure 4e demonstrates the viability of the compensated contact solution, the SEM image suggests that the slightly lower V_{OC} and FF observed in the bottom junction of our

prototype compared to state-of-the-art single-junction devices^{37,39} is probably caused by damage induced in the annealing of the compensated contact, which will be optimized in future prototypes.

Impact of series resistance. Now we discuss another critical aspect in the design of an HBTSC, which is the lateral series resistance of the base layer. Because the current circulating through both junctions travels laterally along the base layer to reach the terminal, each junction suffers from the resistance loss caused by the sum of both currents. The effect of this resistance can be seen in the illuminated J - V curves plotted in Figure 5a, for a test device which was made from the same epitaxial structure used for the HBTSC prototype characterized in Figure 2a, but with a different geometry that results in a higher series resistance opposing the extraction of current through the base. The J - V plots can be found in the SI, Section S11. The larger series resistance in this test device comes from the fact that the maximum distance that majority carriers travel laterally to reach the base terminal is 1.8 mm, to be compared to 0.6 mm in the main HBTSC prototype. It has been shown that the effect of lateral series resistance in HBTSCs can be minimized not only by reducing the current path, as we have done in the prototype presented here, but also through other approaches, such as increasing the base thickness.³³ The most effective strategy to eliminate this problem in practical devices is to use interdigitated bottom contacts, with the base contact fingers aligned below the emitter contact fingers to prevent extra shadowing³⁵ (See SI, Fig. S12). Those fingers can be separated by a distance comparable to the width of our proof-of-concept HBTSC prototype, and the series resistance problem in the base can be treated like it is for conventional emitters.

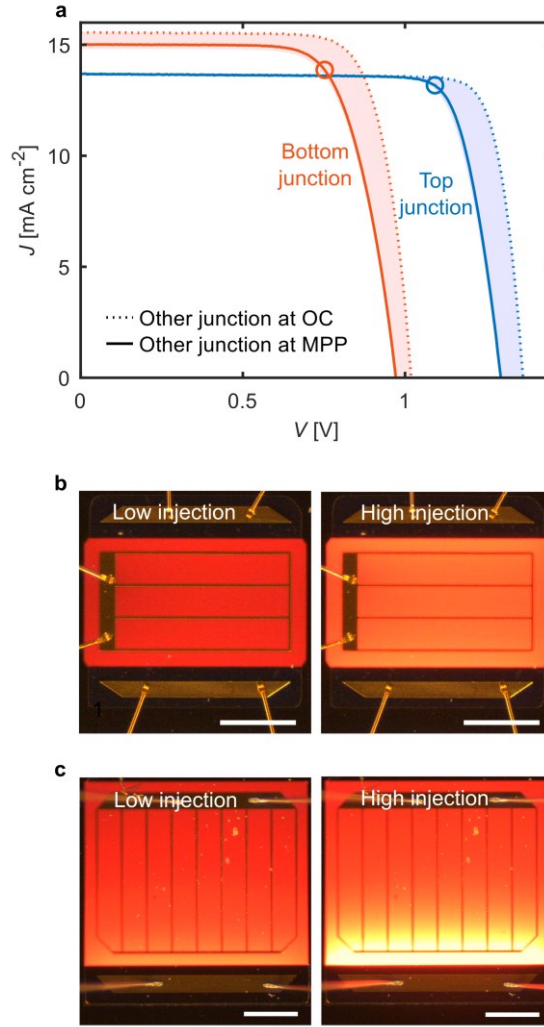


Figure 5. Effect of lateral series resistance. **a**, AM1.5G J - V curves of an HBTSC test device made with the same epitaxial structure as the one characterized in Figure 2a, but with a higher series resistance opposing the extraction of current through the base. V_{OC} s decrease by 74 mV in the top junction and 51 mV in the bottom junction when changing the working point of the not-measured junction from OC to SC. **b-c**, Micrographs showing red electroluminescence from the GaInP top junction. The main HBTSC prototype (**b**) emits uniform light when a current equivalent to one-sun or three-suns photogeneration is injected, whereas the higher resistance test device (**c**) shows a current crowding effect at the base contact when the injected current is equivalent to three-suns. Scale bars are 500 μm long. See also Figure S10.

In Figure 5a, it is apparent that in this test device there is crosstalk between junctions, contrarily to the prototype presented in Fig. 2. In particular, a degradation of the J - V characteristics of both cells when the voltage of the not-measured cell is decreased from OC to SC. Note that not only

the FFs are affected, as in conventional solar cells, but also the V_{OC} s, because at this working point in our device, current from the other junction can circulate through the base. These voltage drops at V_{OC} are 74 mV for the top junction and 51 mV for the bottom junction. We have modeled⁴⁷ the effect of a distributed lateral series resistance by applying the method described by Luque⁵¹ to the geometry of the test device, using a hole mobility in the base of $40 \text{ cm}^2 \text{ V}^{-1} \text{ s}^{-1}$ (in agreement with Ikeda and Kaneko⁵²). We find that the difference between the modelled and measured voltage drops in OC is less than $\pm 13 \text{ mV}$ (see SI Section S9), consistent with the argument that the base lateral resistance is the origin of the observed behavior. For the main HBTSC prototype characterized in Figure 2a, we find that there are barely visible V_{OC} drops of 9 and 6 mV when the not-measured junction is in SC, which are also reproduced when we apply the series resistance model to the geometry of this base layer.

The voltage loss along the current extraction path can be visualized with the help of the photographs in Figure 5. They show the main HBTSC prototype (Figure 5b) and the higher resistance test device (Figure 5c) photographed while a current is injected through their top junction terminals which is equivalent to the respective short-circuit current under one-sun or three-suns illumination. The photographs show red electroluminescence from the top GaInP junction. The device in Figure 5b produces electroluminescence uniformly under the two injection levels, which reflects that the QFL split is homogenous over the whole emitter junction area. In the non-optimized device, the electroluminescence is slightly non-uniform at the lower injection level. This effect is greatly amplified at the higher injection level, for which we observe a current crowding effect that points to a junction voltage that decreases as the distance to the base terminal increases.

Outlook of the optimization of HBTSCs. We have seen that the performance of our proof-of-concept HBTSC prototype is limited by the large areas where the emitter has been etched and by the damage produced in the fabrication of the base contact. As mentioned before, in future devices the epitaxial structure will be detached from the substrate, enabling the implementation of an interdigitated bottom contact for the base terminal as demonstrated in Ref. ³⁵. This strategy circumvents the problem related to lateral series resistance, reduces the shadowing factor to the range which is characteristic of two-terminal devices and enables the scalation of the HBTSC concept to larger areas (see SI, Fig. S12). Also, to avoid V_{OC} and FF degradation, the performance of the compensated contact for the base terminal can be further improved using dry instead of wet etching, which allows for a precise control of the thickness of the compensated layer.

For the interconnection of 3T solar cells into modules, solutions based on voltage-matching have been proposed,^{21,53} and in some cases experimentally tested.⁵⁴⁻⁵⁷ Although they are still under development, these solutions have the potential to outperform 2T-based modules in terms of maximizing energy yield ²¹ and minimizing losses produced by power mismatch among cells ⁵⁵ (e.g. partial shading of the module). It has also been proposed the use of low input DC/DC converters to match the voltage of top and bottom junctions with no current and voltage constraints.⁵⁸ Finally, an approach that would be highly compatible with present photovoltaic technology is to implement a 2T-3JSC comprising an HBTSC (e.g. GaInP/GaAs) attached to, and series-connected to, a silicon bottom cell ⁵⁹ (a schematic can be found in the SI, Section S11). This architecture has a high AM1.5G detailed-balance efficiency (43% for GaInP/GaAs/Si), and despite being 2T, preserves to a great extent the tolerance towards non-optimum E_{GS} and spectral changes typical of 3T architectures because it is based on a parallel/series interconnection.⁵⁹⁻⁶¹ Therefore,

the combination of an HBTSC and a Si cell into a two-terminal device would allow for a high energy yield avoiding a complex stringing that could increase the total manufacturing cost.

Conclusions. We have demonstrated the operation of a three-terminal GaInP/GaAs HBTSC prototype with J - V curves and EQEs comparable to state-of-the-art double-junction solar cells. The difference in output voltage between the top and bottom junctions (380 mV in open circuit under AM1.5G illumination) and the fact that the performance of one junction is independent of the working point of the other, confirm the practical feasibility of this new concept. The operation of the HBTSC relies on the counter-intuitive possibility of using the transistor structure to produce a minority carrier QFL bending, achieving the most compact double-junction device possible, with no isolating layer or tunnel junction between the two junctions. We have also shown that the base layer (565 nm thick, highly-doped GaInP) produces photocurrent that is collected by either junction, and have demonstrated the possibility to fabricate a stable, ohmic contact for this layer. The AM1.5G efficiency achieved by our proof-of-concept prototype is $(27.8 \pm 2.9) \%$ when it is scaled by the illumination areas. We have discussed the impact of lateral series resistance in the base layer, which can compromise the independence of the junctions and degrade the over-all performance of the HBTSC. This problem has been circumvented here by reducing the dimensions of the proof-of-concept prototype, and it can be eliminated in future, large-area devices, with the implementation of a metal grid on the rear of the base layer. Our results open the path to the realization of three-terminal double-junction solar cells with a more compact semiconductor structure than any multi-junction device reported before, which can be used to pursue high-efficiency low-cost PV technologies.

METHODS

Device fabrication. Epitaxial growth on an n-doped (100) GaAs substrate was carried out at NREL in a custom-built metal-organic chemical vapor deposition reactor. The substrate was miscut 2° toward (111)B. Source gases included trimethylgallium, triethylgallium, trimethylindium, trimethylaluminum, arsine and phosphine for the lattice atoms; dimethylhydrazine for the nitrogen in the front contact; disilane, hydrogen selenide, diethylzinc and carbon tetrachloride for the dopants. All growth took place in a purified hydrogen carrier gas flowing at 6 lpm. The substrate was etched in $\text{NH}_4\text{OH}:\text{H}_2\text{O}_2:\text{H}_2\text{O}$ (2:1:10) for 2 minutes before growth and then loaded onto a graphite susceptor in the reactor. Growth began by heating to 700°C under an arsine overpressure and deoxidizing the surface for 10 minutes, followed by 200 nm GaAs and 500 nm AlGaAs seed layers. The temperature was then reduced to 650°C for the semiconductor structure; the front contact layer was grown at 570°C . Growth temperatures were measured using a Type-K thermocouple embedded in the graphite susceptor. The growth rate was $\sim 6 \mu\text{m/hr}$ for the main layers, as determined from calibration samples and from in-situ reflectance measurements using a multibeam optical stress (MOS) sensor (kSpace); the V/III ratio was ~ 85 for the GaAs collector layer and ~ 490 for the GaInP base and emitter layers.

After growth, individual devices were fabricated at IES-UPM using maskless photolithography (SmartPrint by SmartForce, with resist AZ 4562 by Microchemicals) in combination with wet etching, O_2 plasma cleaning (femto PCCE by Diener), metal thermal evaporation (Vaksis with metals from Kurt-Lesker), and thermal annealing (Solaris 75 by SSI). Selective contact layer etching was performed with $\text{NH}_4\text{OH}:\text{H}_2\text{O}_2:\text{H}_2\text{O}$ (2:1:10), 30 s at room temperature. Non-selective GaInP etches were carried out with HCl 12M at a controlled temperature of 3°C , reducing the etch rate to 10-20 nm/s. The metallizations are: Au/Zn/Au⁶³ (15/40/500 nm) for the base contact, AuGe/Ni/Au⁶⁴ (85/25/500 nm) for the emitter contact, and AuGe/Ni/Au⁶⁴ (85/25/300 nm) for the collector contact. All contacts were annealed at 420°C in forming gas for 180 s. Devices were isolated with a mesa etch that reaches $> 200 \text{ nm}$ into the collector layer.

Two batches were processed from the same epitaxial structure, each one containing 18 devices. All devices were tested in the dark and under illumination with probes. Differences in device performance within the same batch were observed which could be attributed to the non-uniformity of the GaInP etch. The best three cells of each batch were cleaved and soldered with indium onto a direct bonded copper (DBC) substrate and two gold wires with 25 μm diameter were bonded on each busbar by ultrasonic welding. An anti-reflection coating of $\text{MgF}_2/\text{ZnS}/\text{MgF}_2$ (5/23/82 nm) was deposited by e-beam evaporation. Devices were stored in normal lab conditions and no degradation was observed over several months of measurements.

Device characterization. EQEs were measured using a lock-in amplifier (Stanford Research SR830) equipped with a transimpedance pre-amplifier (Stanford Research SR570). The light source was a stabilized 100 W quartz tungsten halogen lamp, and the wavelength was selected by a grating monochromator (Cornerstone 260, Newport) equipped with order sorting filters and the slits adjusted to produce a spectral dispersion of 3 nm at the blazing wavelength. No bias light was used for the not-measured junction. To obtain the absolute EQE, the spectral power density of the setup was determined using a NIST-calibrated silicon detector (Newport STPVCERT). Because the HBTSC prototype has a region where the emitter has been etched, it was necessary to compare two devices of different geometry to extract an EQE which is representative of the intact layer structure (plotted in Figure 2d and Figure 2e). This is explained in more detail in the SI, Section S4.

Area measurements were obtained from microphotographs. The area uncertainties are given in the SI, Section S3. They are determined by the irregularity of the etch walls, particularly the GaInP etch. No masks were used to limit the illumination.

J - V curves were measured using source-measure units (B2901A, Keysight). Employing two units, current maps such as the ones plotted in Figure 3a can be performed by sweeping V^{top} and V^{bot} simultaneously. Each sweep covered a range of 1.5 V and included 50 points, spaced following a logarithmic series so that the density is higher around MPP and V_{OC} . The integration time was 0.08

s (4 power-line cycles at 50 Hz) and the scan speed ~ 0.35 V/s. From those maps, J - V curves of either junction such as the ones depicted in Figure 2a, can be easily extracted.

An LED-based sun simulator (LS-2, Wavelabs; calibrated 8/2020) was used as illumination source for the J - V maps. The simulator produces a factory-calibrated AM1.5G spectrum⁶⁵ with AAA quality and a one-Sun irradiance of $100 \text{ mW}\cdot\text{cm}^{-2}$. The irradiance was fine adjusted by tweaking the distance between the LED plane and the sample platform using a calibrated Si solar cell (Newport SRC-1000-TC-K-QZ-N, calibrated 9/2011). It was verified that the difference between the short-circuit currents produced by the HBTSC under the solar simulator after this calibration and the values obtained from the integration of the respective experimental absolute EQEs over the AM1.5G spectrum was $< 5\%$. Then, to correct for spectral mismatch the intensity of the LEDs closest in energy to the E_G of GaInP and GaAs was fine tuned to match the photocurrents of either junction simultaneously to the values obtained from the EQEs integrated over the AM1.5G spectrum. The HBTSC device was measured in open air on a vacuum hold-down stage and kept at 25°C with a closed-loop temperature controller. No hysteresis was observed in the J - V curves. The main components in the efficiency uncertainty ($\sim 10\%$) are the area measurement error (up to 7%) and, to a lesser extent, the long-term instability of the solar simulator power density over the long measurement of J - V maps (2%).

The J - V curves of the bottom junction showed luminescent coupling, but the EQEs obtained with the described setup when the non-measured junction was in SC and OC were identical. An additional measurement of the EQE was performed using the LED-based solar simulator by powering one wavelength at a time. In this measurement, shown in the SI Section S6, the EQE of the bottom junction is slightly higher in the < 700 nm wavelength range when the top cell is in OC than when it is in SC. This is consistent with the presence of photon coupling, which is observed only under sufficient illumination of the top junction. In the EQE measurement with the LED simulator the illumination density is ~ 80 mW per wavelength, whereas in the measurement with the monochromator it is $< 0.1 \text{ mW}\cdot\text{cm}^{-2}\cdot\text{nm}^{-1}$. When measuring the AM1.5G J - V curves under the

solar simulator our correction for spectral mismatch based on the integration of the EQE was not affected by luminescent coupling because it was performed when both cells were in SC.

Theoretical modelling. To model the EQE, we first calculated the photon flux at different depths inside the structure by applying the generalized matrix method as described by E. Centurioni,⁶⁶ with refractive indexes taken from Aspnes *et al.*⁶⁷ and Ochoa-Martínez *et al.*⁶⁸ In this context, the photon flux at a given point x is the total fraction of photons from an arbitrary initial flux impinging the front of the structure that propagate through point x , including photons that have been reflected at the interfaces and taking into account their interference. The wavelength-dependent light flux at the interfaces between layers is particularly important because it will be used in the EQE model. From this calculation it is also possible to obtain the integrated absorptance of each layer, which is shown in the SI, Section S5. Then, to calculate the collection of photocurrent we solved the one-dimensional continuity equations for minority carriers assuming low-injection and quasi-neutrality, adapting the approach proposed by Hovel⁴⁸ for single-junction solar cells to the layer structure of an HBTSC. The minority carrier continuity equations were solved at the borders of each semiconductor region, obtaining the density of excess carriers (Δn) photogenerated from the absorption of the light flux at that point with a specific wavelength (λ). The EQE was then calculated from the equation $EQE(\lambda) = D \left. \frac{d\Delta n}{dx} \right|_{x=x_0}$, where D is the minority carrier diffusion constant, and x_0 is the position of the layer border. The equations were solved symbolically, not numerically, using the Sympy⁶⁹ Python library in the open-source Jupyter Notebook⁷⁰ environment. Our code for solving the minority carrier continuity equations in the HBTSC is available in GitHub.⁴⁷

The effect of the base lateral series resistance on the J - V curves was modelled by applying the method described by A. Luque⁵¹ to the geometry of our devices. In this method, a lumped resistance expression is obtained for those elements of the device that have a distributed resistance (emitter, base, front metal grid, etc.) through the calculation of the power dissipated in them. The equations are given in the SI, Section S9.

DATA AVAILABILITY:

The datasets generated and/or analyzed during the current study are available at Zenodo, see Ref. ⁶².

CODE AVAILABILITY:

The code for the HBTSC quantum efficiency modelling, the optical model and the series resistance model is available in GitHub, see Ref. ⁴⁷.

REFERENCES

1. Shockley, W., and Queisser, H.J. (1961). Detailed Balance Limit of Efficiency of p-n Junction Solar Cells. *J. Appl. Phys.* *32*, 510–519.
2. Wolf, M. (1960). Limitations and Possibilities for Improvement of Photovoltaic Solar Energy Converters: Part I: Considerations for Earth’s Surface Operation. *Proc. IRE* *48*, 1246–1263.
3. Martí, A. (2019). Limiting Efficiency of Heterojunction Solar Cells. *IEEE J. Photovolt.* *9*, 1590–1595.
4. Jackson, E.D. (1958). Areas for Improvement of the Semiconductor Solar Energy Converter. In (University of Arizona Press), pp. 122–126.
5. Kurtz, S.R., Faine, P., and Olson, J.M. (1990). Modeling of two-junction, series-connected tandem solar cells using top-cell thickness as an adjustable parameter. *J. Appl. Phys.* *68*, 1890–1895.
6. García, I., Rey-Stolle, I., Galiana, B., and Algora, C. (2009). A 32.6% efficient lattice-matched dual-junction solar cell working at 1000 suns. *Appl. Phys. Lett.* *94*, 053509.
7. Flores, C. (1983). A three-terminal double junction GaAs/GaAlAs cascade solar cell. *IEEE Electron Device Lett.* *4*, 96–99.
8. Steiner, M.A., Wanlass, M.W., Carapella, J.J., Duda, A., Ward, J.S., Moriarty, T.E., and Emery, K.A. (2009). A Monolithic Three-Terminal GaInAsP/GaInAs Tandem Solar Cell. *Prog. Photovolt.* *17*, 587–593.

9. Wanlass, M.W., Ward, J.S., Emery, K.A., Gessert, T.A., Osterwald, C.R., and Coutts, T.J. (1991). High-performance concentrator tandem solar cells based on IR-sensitive bottom cells. *Sol. Cells* 30, 363–371.
10. Martí, A., and Luque, A. (2015). Three-terminal heterojunction bipolar transistor solar cell for high-efficiency photovoltaic conversion. *Nat. Commun.* 6, 6902.
11. Antolín, E., Zehender, M.H., García-Linares, P., Svatek, S.A., and Martí, A. (2020). Considerations for the Design of a Heterojunction Bipolar Transistor Solar Cell. *IEEE J. Photovolt.* 10, 2–7.
12. Geisz, J.F., France, R.M., Schulte, K.L., Steiner, M.A., Norman, A.G., Guthrey, H.L., Young, M.R., Song, T., and Moriarty, T. (2020). Six-junction III–V solar cells with 47.1% conversion efficiency under 143 Suns concentration. *Nat. Energy* 5, 326–335.
13. Sahli, F., Werner, J., Kamino, B.A., Bräuninger, M., Monnard, R., Paviet-Salomon, B., Barraud, L., Ding, L., Leon, J.J.D., Sacchetto, D., et al. (2018). Fully textured monolithic perovskite/silicon tandem solar cells with 25.2% power conversion efficiency. *Nat. Mater.* 17, 820–826.
14. Köhnen, E., Jošt, M., Morales-Vilches, A.B., Tockhorn, P., Al-Ashouri, A., Macco, B., Kegelmann, L., Korte, L., Rech, B., Schlatmann, R., et al. (2019). Highly efficient monolithic perovskite silicon tandem solar cells: analyzing the influence of current mismatch on device performance. *Sustain. Energy Fuels* 3, 1995–2005.
15. Cariou, R., Benick, J., Feldmann, F., Höhn, O., Hauser, H., Beutel, P., Razeq, N., Wimplinger, M., Bläsi, B., Lackner, D., et al. (2018). III–V-on-silicon solar cells reaching 33% photoconversion efficiency in two-terminal configuration. *Nat. Energy* 3, 326–333.
16. Schulte-Huxel, H., Silverman, T.J., Deceglie, M.G., Friedman, D.J., and Tamboli, A.C. (2018). Energy Yield Analysis of Multiterminal Si-Based Tandem Solar Cells. *IEEE J. Photovolt.* 8, 1376–1383.
17. Warren, E.L., Deceglie, M.G., Rienäcker, M., Peibst, R., Tamboli, A.C., and Stradins, P. (2018). Maximizing tandem solar cell power extraction using a three-terminal design. *Sustain. Energy Fuels* 2, 1141–1147.
18. Ripalda, J.M., Buencuerpo, J., and García, I. (2018). Solar cell designs by maximizing energy production based on machine learning clustering of spectral variations. *Nat. Commun.* 9, 5126.
19. Villa, J., and Martí, A. (2017). Impact of the Spectrum in the Annual Energy Production of Multijunction Solar Cells. *IEEE J. Photovolt.* 7, 1479–1484.
20. Hörantner, M.T., and Snath, H.J. (2017). Predicting and optimising the energy yield of perovskite-on-silicon tandem solar cells under real world conditions. *Energy Environ. Sci.* 10, 1983–1993.

21. Schulte-Huxel, H., Friedman, D.J., and Tamboli, A.C. (2018). String-Level Modeling of Two, Three, and Four Terminal Si-Based Tandem Modules. *IEEE J. Photovolt.* 8, 1370–1375.
22. Essig, S., Allebé, C., Remo, T., Geisz, J.F., Steiner, M.A., Horowitz, K., Barraud, L., Ward, J.S., Schnabel, M., Descoedres, A., et al. (2017). Raising the one-sun conversion efficiency of III–V/Si solar cells to 32.8% for two junctions and 35.9% for three junctions. *Nat. Energy* 2, 17144.
23. Rienäcker, M., Warren, E.L., Schnabel, M., Schulte-Huxel, H., Niepelt, R., Brendel, R., Stradins, P., Tamboli, A.C., and Peibst, R. (2019). Back-contacted bottom cells with three terminals: Maximizing power extraction from current-mismatched tandem cells. *Prog. Photovolt. Res. Appl.*
24. Haas, A.W., Wilcox, J.R., Gray, J.L., and Schwartz, R.J. (2011). Design of a GaInP/GaAs tandem solar cell for maximum daily, monthly, and yearly energy output. *J. Photonics Energy* 1, 018001.
25. Jain, N., Schulte, K.L., Geisz, J.F., Friedman, D.J., France, R.M., Perl, E.E., Norman, A.G., Guthrey, H.L., and Steiner, M.A. (2018). High-efficiency inverted metamorphic 1.7/1.1 eV GaInAsP/GaInAs dual-junction solar cells. *Appl. Phys. Lett.* 112, 053905.
26. Metaferia, W., Schulte, K.L., Simon, J., Johnston, S., and Ptak, A.J. (2019). Gallium Arsenide Solar Cells Grown at Rates Exceeding $300 \mu\text{m h}^{-1}$ by Hydride Vapor Phase Epitaxy. *Nat. Commun.* 10, 3361.
27. Schulte, K.L., Simon, J., Young, M.R., and Ptak, A.J. (2018). Improvement of Short-Circuit Current Density in GaInP Solar Cells Grown by Dynamic Hydride Vapor Phase Epitaxy. *IEEE J. Photovolt.* 8, 1616–1620.
28. Yoon, J., Jo, S., Chun, I.S., Jung, I., Kim, H.-S., Meitl, M., Menard, E., Li, X., Coleman, J.J., Paik, U., et al. (2010). GaAs photovoltaics and optoelectronics using releasable multilayer epitaxial assemblies. *Nature* 465, 329–333.
29. Linares, P.G., Antolín, E., and Martí, A. (2019). Novel heterojunction bipolar transistor architectures for the practical implementation of high-efficiency three-terminal solar cells. *Sol. Energy Mater. Sol. Cells* 194, 54–61.
30. Saha, U., and Alam, Md.K. (2019). A heterojunction bipolar transistor architecture-based solar cell using CBTSSe/CdS/ACZTSe materials. *Sol. Energy* 184, 664–671.
31. Giliberti, G., Martí, A., and Cappelluti, F. (2020). Perovskite-Si solar cell: a three-terminal heterojunction bipolar transistor architecture. In 2020 47th IEEE Photovoltaic Specialists Conference (PVSC), pp. 2696–2699.
32. Wahid, S., and Alam, Md.K. (2020). Efficiency Enhancement of Perovskite Solar Cells Using Heterojunction Bipolar Transistor Configuration. *IEEE Trans. Electron Devices* 67, 552–557.

33. Zehender, M.H., García, I., Svatek, S.A., Steiner, M.A., García-Linares, P., Warren, E., Tamboli, A., Martí, A., and Antolín, E. (2019). Demonstrating the GaInP/GaAs Three-Terminal Heterojunction Bipolar Transistor Solar Cell. In 2019 IEEE 46th Photovoltaic Specialists Conference (PVSC), pp. 0035–0040.
34. Cich, M.J., Johnson, J.A., Peake, G.M., and Spahn, O.B. (2003). Crystallographic dependence of the lateral undercut wet etching rate of InGaP in HCl. *Appl. Phys. Lett.* *82*, 651–653.
35. Zehender, M.H., Svatek, S.A., Steiner, M.A., García, I., Linares, P.G., Warren, E.L., Martí, A., Tamboli, A.C., and Antolín, E. (2020). Inverted GaInP/GaAs Three-Terminal Heterojunction Bipolar Transistor Solar Cell. In 2020 47th IEEE Photovoltaic Specialists Conference (PVSC), pp. 1517–1521.
36. Warren, E.L., McMahon, W.E., Rienäcker, M., VanSant, K.T., Whitehead, R.C., Peibst, R., and Tamboli, A.C. (2020). A Taxonomy for Three-Terminal Tandem Solar Cells. *ACS Energy Lett.* *5*, 1233–1242.
37. Kayes, B.M., Nie, H., Twist, R., Spruytte, S.G., Reinhardt, F., Kizilyalli, I.C., and Higashi, G.S. (2011). 27.6% Conversion efficiency, a new record for single-junction solar cells under 1 sun illumination. In.
38. Geisz, J.F., Steiner, M.A., García, I., Kurtz, S.R., and Friedman, D.J. (2013). Enhanced external radiative efficiency for 20.8% efficient single-junction GaInP solar cells. *Appl. Phys. Lett.* *103*, 041118.
39. Green, M.A., Dunlop, E.D., Levi, D.H., Hohl-Ebinger, J., Yoshita, M., and Ho-Baillie, A.W.Y. (2019). Solar cell efficiency tables (version 54). *Prog. Photovolt. Res. Appl.* *27*, 565–575.
40. Schnabel, M., Rienäcker, M., Warren, E.L., Geisz, J.F., Peibst, R., Stradins, P., and Tamboli, A.C. (2018). Equivalent Performance in Three-Terminal and Four-Terminal Tandem Solar Cells. *IEEE J. Photovolt.* *8*, 1584–1589.
41. Steiner, M.A., and Geisz, J.F. (2012). Non-linear luminescent coupling in series-connected multijunction solar cells. *Appl. Phys. Lett.* *100*, 251106.
42. Lim, S.H., Li, J.-J., Steenbergen, E.H., and Zhang, Y.-H. (2013). Luminescence coupling effects on multijunction solar cell external quantum efficiency measurement. *Prog. Photovolt. Res. Appl.* *21*, 344–350.
43. Steiner, M.A., Geisz, J.F., Moriarty, T.E., France, R.M., McMahon, W.E., Olson, J.M., Kurtz, S.R., and Friedman, D.J. (2012). Measuring IV curves and subcell photocurrents in the presence of luminescent coupling. In 2012 IEEE 38th Photovoltaic Specialists Conference (PVSC) PART 2, pp. 1–11.
44. Luque, A., and Martí, A. (2011). Theoretical Limits of Photovoltaic Conversion and New-Generation Solar Cells. In *Handbook of Photovoltaic Science and Engineering* (Chap. 4, Eds. A. Luque and S. Hegedus, John Wiley & Sons, Chichester), pp. 130–168.

45. Martí, A., Antolín, E., García-Linares, P., López, E., Villa, J., and Ramiro, I. (2017). Operation of the Three Terminal Heterojunction Bipolar Transistor Solar Cell. *Phys. Status Solidi C* *14*, 1700191.
46. Green, M.A., Hishikawa, Y., Dunlop, E.D., Levi, D.H., Hohl-Ebinger, J., and Ho-Baillie, A.W.Y. (2018). Solar cell efficiency tables (version 51). *Prog. Photovolt. Res. Appl.* *26*, 3–12.
47. Marti, A., Antolín, E., Zehender, M.H., Ramiro, I., and Svatek, S.A. (2020). Modelling the 3T-Heterojunction Bipolar Transistor Solar Cell in GitHub. https://github.com/amartiv/3_Terminal_Transistor_Solar_Cell.
48. Hovel, H.J. (1975). *Solar cells* (Acad. Press).
49. Kamińska, E., Piotrowska, A., Barcz, A., and Adamczewska, J. (1986). Interaction of Au/Zn/Au sandwich contact layers with AIIIIV compound semiconductors. *Solid-State Electron.* *29*, 279–286.
50. Malina, V., Vogel, K., Ressel, P., Pécz, B., and Dobos, L. (2001). Related Electrical and Metallurgical Properties of Pd/Zn/Pd/Ge and Pd/Zn/Pd/Au Contact Systems to p-InGaP. *Phys. Status Solidi A* *184*, 139–144.
51. Luque, A., and Araújo, G.L. (1989). *Solar cells and optics for photovoltaic concentration* (A. Hilger).
52. Ikeda, M., and Kaneko, K. (1989). Selenium and zinc doping in Ga_{0.5}In_{0.5}P and (Al_{0.5}Ga_{0.5})_{0.5}In_{0.5}P grown by metalorganic chemical vapor deposition. *J. Appl. Phys.* *66*, 5285–5289.
53. Gee, J.M. (1988). A comparison of different module configurations for multi-band-gap solar cells. *Sol. Cells* *24*, 147–155.
54. Zehender, M., Antolín, E., García-Linares, P., Artacho, I., Ramiro, I., Villa, J., and Martí, A. (2018). Module interconnection for the three-terminal heterojunction bipolar transistor solar cell. *AIP Conf. Proc.* *2012*, 040013.
55. Witteck, R., Blankemeyer, S., Siebert, M., Köntges, M., and Schulte-Huxel, H. (2021). Partial shading of one solar cell in a photovoltaic module with 3-terminal cell interconnection. *Sol. Energy Mater. Sol. Cells* *219*, 110811.
56. McMahon, W.E., Schulte-Huxel, H., Buencuerpo, J., Geisz, J.F., Young, M.S., Klein, T.R., Tamboli, A.C., and Warren, E.L. (2021). Homogenous Voltage-Matched Strings Using Three-Terminal Tandem Solar Cells: Fundamentals and End Losses. *IEEE J. Photovolt.* *11*, 1078–1086.
57. Geisz, J.F., McMahon, W.E., Buencuerpo, J., Rienäcker, M., Tamboli, A.C., and Warren, E.L. Unique Characterization of Three-Terminal Photovoltaic Devices. Under review at Joule.

58. Martí, A., García-Linares, P., Zehender, M., Svatek, S.A., Artacho, I., Cristóbal, A.B., González, J.R., Baur, C., Ramiro, Í., Cappelluti, F., et al. (2019). Potential of the three-terminal heterojunction bipolar transistor solar cell for space applications. In 2019 European Space Power Conference (ESPC), pp. 1–5.
59. Antolín, E., Zehender, M.H., Svatek, S.A., García-Linares, P., and Martí, A. (2020). III-V-on-silicon triple-junction based on the heterojunction bipolar transistor solar cell concept. In 2020 47th IEEE Photovoltaic Specialists Conference (PVSC), pp. 1226–1231.
60. Guo, F., Li, N., Fecher, F.W., Gasparini, N., Quiroz, C.O.R., Bronnbauer, C., Hou, Y., Radmilović, V.V., Radmilović, V.R., Spiecker, E., et al. (2015). A generic concept to overcome bandgap limitations for designing highly efficient multi-junction photovoltaic cells. *Nat. Commun.* *6*, 7730.
61. Trupke, T., and Würfel, P. (2004). Improved spectral robustness of triple tandem solar cells by combined series/parallel interconnection. *J. Appl. Phys.* *96*, 2347–2351.
62. Marius H. Zehender, Simon A. Svatek, Myles A. Steiner, Iván García, Pablo García-Linares, Emily L. Warren, Adele C. Tamboli, Antonio Martí, and Elisa Antolín (2021). Dataset for GaInP/GaAs three-terminal heterojunction bipolar transistor solar cell. (Version 1) [Data set]. Zenodo. DOI: 10.5281/zenodo.4767678.
63. Lu, Y., Kalkur, T.S., and Araujo, C.A.P. de (1989). *J. Electrochem. Soc.* *136*, 3123–3129.
64. Bruce, R.A., and Piercy, G.R. (1987). An improved Au-Ge-Ni ohmic contact to n-type GaAs. *Solid-State Electron.* *30*, 729–737.
65. ASTM (2012). G173-03, Standard Tables for Reference Solar Spectral Irradiances: Direct Normal and Hemispherical on 37° Tilted Surface, ASTM International, West Conshohocken, PA.
66. Centurioni, E. (2005). Generalized matrix method for calculation of internal light energy flux in mixed coherent and incoherent multilayers. *Appl. Opt.* *44*, 7532.
67. Aspnes, D.E., Kelso, S.M., Logan, R.A., and Bhat, R. (1986). Optical properties of $\text{Al}_x\text{Ga}_{1-x}\text{As}$. *J. Appl. Phys.* *60*, 754–767.
68. Ochoa-Martínez, E., Barrutia, L., Ochoa, M., Barrigón, E., García, I., Rey-Stolle, I., Algora, C., Basa, P., Kronome, G., and Gabás, M. (2018). Refractive indexes and extinction coefficients of n- and p-type doped GaInP, AlInP and AlGaInP for multijunction solar cells. *Sol. Energy Mater. Sol. Cells* *174*, 388–396.
69. Meurer, A., Smith, C.P., Paprocki, M., Čertík, O., Kirpichev, S.B., Rocklin, M., Kumar, Am., Ivanov, S., Moore, J.K., Singh, S., et al. (2017). SymPy: symbolic computing in Python. *PeerJ Comput. Sci.* *3*, e103.
70. Kluyver, T., Ragan-Kelley, B., Pérez, F., Granger, B., Bussonnier, M., Frederic, J., Kelley, K., Hamrick, J., Grout, J., Corlay, S., et al. (2016). Jupyter Notebooks – a publishing format for

reproducible computational workflows. In *Positioning and Power in Academic Publishing: Players, Agents and Agendas*, F. Loizides and B. Schmidt, eds. (IOS Press), pp. 87–90.

ACKNOWLEDGMENTS

This work has been funded by the Ministry of Science and Innovation of Spain through the Multiplier Project (RTI2018-096937-B-C21) and by the European Union’s Horizon2020 Research and Innovation Programme under grant agreement 787289. The authors would like to thank Prof. Ignacio Tobías from IES-UPM for help with the optical modeling, Irene Artacho and Miguel Gómez from IES-UPM for technical support, and Andrés Velasco y Javier Martínez from ISOM-UPM for help with SEM measurements. M.H.Z. is grateful to Universidad Politécnica de Madrid for funding from the ‘Programa Propio para Ayudas Predoctorales de la UPM’. E.A. acknowledges a Ramón y Cajal Fellowship (RYC-2015-18539) funded by the Ministry of Science and Innovation of Spain. E.A. is also grateful to the Iberdrola Foundation for their funding through the ConCEPT grant. This work was co-authored by Alliance for Sustainable Energy, LLC, the manager and operator of the National Renewable Energy Laboratory for the U.S. Department of Energy (DOE) under Contract No. DE-AC36-08GO28308. The authors would like to thank Waldo Olavarria for help with MOCVD growth. Funding provided by the Office of Energy Efficiency and Renewable Energy, Solar Energy Technology Office under contracts DE-00034911 and DE-00034358. The views expressed in the article do not necessarily represent the views of the DOE or the U.S. Government. The U.S. Government retains and the publisher, by accepting the article for publication, acknowledges that the U.S. Government retains a nonexclusive, paid-up, irrevocable, worldwide license to publish or reproduce the published form of this work, or allow others to do so, for U.S. Government purposes.

AUTHOR CONTRIBUTIONS

E.A. conceived the project and designed the samples. M.A.S. designed the MOCVD growth recipes of the semiconductor structure. M.H.Z. designed the metallization grid, and fabricated the devices with help of S.A.S. I.G. deposited the ARC. P.G-L contributed to the development of metallizations. M.H.Z. performed the EQE characterization with the help of I.G. S.A.S and M.H.Z developed the J - V - V characterization method, and M.H.Z. performed the experiments. A.M, M.H.Z, E.A., and S.A.S developed the theoretical models. M.A.S., E.L.W and A.C.T. contributed to the analysis of the 3T behavior. E.A. supervised the project. E.A. and M.H.Z. wrote the first draft of the manuscript. All authors discussed the results and contributed to the final version of the manuscript.

COMPETING INTERESTS

The authors declare no competing interests.

MATERIALS & CORRESPONDENCE:

This study did not generate new unique reagents.

elisa.antolin@upm.es

Group website: www.ies.upm.es/Investigacion/IES_GI/SyNC

SUPPLEMENTARY INFORMATION

S1: Complete layer structure and doping profiling (SIMS)

S2: Supplementary band diagrams

S3: Device geometry and efficiency calculations

S4: Supplementary EQE data

S5: Modelling of optical absorption

S6: Supplementary characterization of luminescent coupling

S7: Dark J - V curves

S8: SIMS profile of compensated contact

S9: Series resistance model

S10: Voltage maps of the test device

S11: 2T HBTSC-on-Si architecture

S12: Top interdigitated and bottom interdigitated base contact

Supplementary Files

This is a list of supplementary files associated with this preprint. Click to download.

- [SIGalnPHBTSCPoCdef3.pdf](#)